A new parameterization of coastal drag to simulate landfast ice in deep marginal seas in the Arctic

Yuqing Liu[1], Martin Losch[1], Nils Hutter[1,2], Longjiang Mu[3]

[1]Alfred-Wegener-Institut, Helmholtz-Zentrum für Polar-und Meeresforschung, Bremerhaven, Germany
[2]Cooperative Institute for Climate, Ocean and Ecosystem Studies, University of Washington, Seattle, WA, USA
[3]Pilot National Laboratory for Marine Science and Technology, Qingdao, China

Key Points:

- In a new landfast ice parameterization, static friction describes the lateral drag between sea ice and the coast.
- The new parameterization improves landfast ice simulation in the Arctic, especially in the Kara Sea.
- The results suggest that multiple mechanisms are at work to create and maintain landfast ice in marginal seas.

Corresponding author: Yuqing Liu, `yuqing.liu@awi.de`

Abstract

Landfast ice is nearly immobile sea ice attached to the coast. Landfast ice inhibits atmosphere-ocean fluxes of heat, moisture, and momentum, leads to offshore flaw polynyas, and stores fresh river water in wintertime. Despite these important roles in coastal environments, landfast ice is not well simulated in current sea ice models, because landfast ice dynamics differ from the pack ice in the interior Arctic and require explicit parameterization. The dynamical mechanisms for landfast ice formation are linked to the local geography. Grounded ice ridges act as anchor points in shallow water. Coastlines and offshore island chains may also be pinning points between which arches of landfast ice can form in deep water. The grounding mechanism for landfast ice in shallow marginal seas has been successfully parameterized using bathymetry information, but this grounding scheme fails in deep regions. We describe a new landfast ice parameterization that uses lateral drag as a function of sea ice thickness, drift velocity, and local coastline length. The simulated landfast ice in a 36 km pan-Arctic sea ice-ocean simulation is compared to observations from satellite data and the effect of the new lateral drag parameterization is evaluated. The combination of the established grounding scheme for shallow water and the new lateral drag parameterization for deep water leads to an improved and realistic landfast ice distribution in most marginal seas in the Arctic. These results suggest that multiple mechanisms are at work to create and maintain landfast ice in marginal seas.

Plain Language Summary

Landfast ice is sea ice that is attached to the coast and nearly stationary. In the Arctic, the stable landfast ice cover along the coasts of the marginal seas serves local communities for traveling and hunting, and provides habitat for Arctic wildlife. Two main processes lead to landfast ice: grounding of ice in shallow water, and anchoring to pinning points such as islands in the deep water. However, sea ice and ocean models to study the Arctic climate typically do not predict the distribution of landfast ice very well. Here, we present a new approach to representing the pinning effect of coastlines and islands. In our improved model, sea ice tends to stick to the coast and is more similar to observed landfast ice. We conclude that the new method will improve future projections of landfast ice in the Arctic that may prove useful for Arctic communities and wildlife management.

1 Introduction

Landfast ice is defined as "sea ice that stays fast along the coast where it is attached to the shore, to an ice wall, to an ice front, or over shoals, or between grounded icebergs." (World Meteorological Organization, 1970). Landfast ice is a common phenomenon in polar winter. It forms in the autumn as onshore winds thicken and consolidate the ice along the shore until it breaks up in spring. The extent of landfast ice in the Arctic varies with water depth and slope of the continental shelf (Yu et al., 2014; Kwok, 2018). Anchored pressure ridges ground coastal sea ice in shallow water all along the coast of Alaska and the Laptev Sea. Landfast ice can also be formed in deep marginal regions by lateral propagation of internal stresses from contact points with the coastline, as seen in the Kara Sea (Li et al., 2020). Furthermore, landfast ice can also be landlocked ice that is confined in the narrow channels of the Canadian Arctic Archipelago (Melling, 2002; Howell et al., 2016). In Antarctica, where the bathymetric features are very different from the Arctic, landfast ice can be found in 400–500 meter deep water, pinned by grounded icebergs (Massom et al., 2001; Fraser et al., 2012, 2020).

Landfast ice is an important player in Arctic and Antarctic coastal environments. It forms a stable cover that decreases the transfer of heat, moisture, and momentum between the atmosphere and the ocean (Johnson et al., 2012; Lemieux et al., 2016). As a consequence, ocean mixing is generally reduced underneath a landfast ice cover. The stable cover also limits further ice growth and hence reduces salt rejection (Eicken et al., 2005). Landfast ice closes coastal polynyas and, instead, results in offshore flaw polynyas or flaw leads (the openings between the landfast ice and pack ice) with consequences for the thermocline circulation in the Arctic (Itkin et al., 2015). In Antarctica, landfast ice connects the Antarctic ice sheet and the ocean, stabilizes ice shelves, delays ice-berg calving, and affects the ice sheet mass balance (Massom & Stammerjohn, 2010; Massom et al., 2018; Greene et al., 2018). Landfast ice is also important for coastal communities in the Arctic. As a seasonal land extension, landfast ice can be a habitat for polar animals and serves as a platform for hunting, fishing, and scientific observation (Kooyman & Ponganis, 2014). The distribution of landfast ice is also important for polar navigation and offshore exploration (Hughes et al., 2011; Zhao et al., 2020). A model without landfast ice (parameterized or resolved) will also have difficulties in simulating the processes related to landfast ice, and for example will have polynyas in the wrong place (Itkin et al., 2015). Finally, landfast ice is likely a sensitive indicator of climate change (Mahoney et al., 2007).

The life cycle of landfast ice is primarily determined by the thermodynamic processes due to the limited horizontal movement of landfast ice (Flato & Brown, 1996; Selyuzhenok et al., 2015). The combined effects of dynamical movement and thermodynamic melting, however, lead to landfast ice break-up (Leppäranta, 2013; Selyuzhenok et al., 2015; Zhai et al., 2021). Here we focus on the dynamics of landfast ice for two reasons. First, the main challenges of modeling landfast ice are maintaining stability during the landfast ice season under continuous dynamical forcing from the surface winds and ocean currents and the timing of the break-up of landfast ice; i.e., initiating the breakdown of the stability at the right time towards the end of the season with the same parameterized dynamics. Second, even small horizontal movement of sea ice leads to a considerable lateral drag because the contact area between sea ice and the coastlines or islands is large. Small changes of this drag are expected to contribute to the break-up of landfast ice.

Most large-scale sea ice models underestimate the extent of landfast ice (Lemieux et al., 2018). Several attempts have been made to improve the simulation of landfast ice in these models. Beatty and Holland (2010) added isotropic tensile strength to a viscous-plastic sea ice model (Hibler, 1979) to simulate landfast ice. Itkin et al. (2015) simulated landfast ice by adding tensile strength to the sea ice rheology in regions shallower than 25 m, and found that landfast ice affected the stability of the halocline in the Arctic. Olason (2016) was able to simulate landfast ice in the Kara Sea by increasing the maximum sea ice viscosity, a parameter that regularizes the momentum equation of sea ice, but left the appropriate value of maximum viscosity an open question. Olason (2016) also reported that the landfast ice in the Kara Sea was primarily supported by static arching, which was consistent with observations suggesting that a chain of offshore islands provides anchor points for the landfast ice in the Kara Sea (Divine et al., 2005). Lemieux et al. (2015) parameterized grounding of ice keels by a basal drag term as a function of topography and sea ice thickness to enhance the representation of landfast ice in shallow water. This grounding scheme is also called basal drag parameterization. Lemieux et al. (2016) used a combination of this basal drag parameterization and increased tensile strength to enhance the simulation of landfast ice extent in deep water, but the simulated landfast ice seasons for the Kara Sea were still too short compared to the satellite data. Note that adding tensile strength or changing sea ice strength modifies the sea ice rheology in the entire Arctic. Furthermore, the basal drag parameterization systematically underestimates the landfast ice extent in the deep water where ice ridge keels cannot reach the bottom.

In this study, we parameterize the effects of partly unresolved coastlines and islands as obstacles to sea ice motion by a lateral drag term in the sea ice momentum equation, with the goal of improved landfast ice representation in the Arctic. We test different approaches to explore the best representation of the lateral drag. As in previous studies (Lemieux et al., 2015, 2016; Olason, 2016), we focus on the Arctic marginal seas, in particular the Kara Sea. The landlocked landfast ice in the Canadian Arctic Archipelago is governed by different dynamics and requires different parameterizations (Lemieux et al., 2018), and is not addressed in the present study.

The paper is organized as follows: the model configuration and experiment setup are described in Section 2, the lateral drag parameterization is shown in Section 3, the model results are presented in Section 4, and the discussion and summary are given in Section 5 and Section 6, respectively.

2 Data and model simulations

2.1 Satellite observations

We used landfast ice records of satellite data from the National Ice Center (NIC) Arctic Sea Ice Charts and Climatologies (U. S. National Ice Center, 2006, updated 2009). The data are available as one week (January 1972 through June 2001) and two week averages (July 2001 through December 2007) on a 25 km Equal-Area Scalable Earth Grid. The sea ice concentration (SIC) ranges from 0% to 100% with landfast ice flagged. NIC charts are produced by manual analysis of in situ, air reconnaissance and remote sensing data, and model output. We chose the biweekly data set and the period from 2001 to 2007 for a straightforward comparison to previous landfast ice modeling results that use the same data set (Lemieux et al., 2015, 2016).

2.2 Model simulations

All simulations in this paper are based on a regional Arctic configuration of the Massachusetts Institute of Technology general circulation model (MITgcm, Marshall et al., 1997; MITgcm Group, 2009) with a grid resolution of 36 km, similar to the configuration of Ungermann and Losch (2018). This configuration applies zero-layer thermodynamics and viscous-plastic dynamics with the solver introduced by Zhang and Hibler (1997). The model is forced by six-hourly atmospheric fields from the European Centre for Medium-Range Weather Forecasts (ECMWF) ERA-Interim data (Dee et al., 2011). The hydrography is initialized with temperature and salinity fields from the Polar Science Center Hydrographic Climatology 3.0 (PHC-3.0, Steele et al., 2001). Details of the sea ice model can be found in Losch et al. (2010) or the online documentation (`https://mitgcm.org`).

The model solves the two-dimensional sea ice momentum equation:

$$m\frac{\partial \mathbf{u}}{\partial t} = -mf\mathbf{k}\times\mathbf{u} + \boldsymbol{\tau}_a + \boldsymbol{\tau}_o + \boldsymbol{\tau}_b + \boldsymbol{\tau}_l - mg\Delta\,H + \nabla\cdot\boldsymbol{\sigma}, \tag{1}$$

where $m = \rho_i h$ is sea ice mass per grid cell area and h is the grid-cell averaged mean ice thickness, i.e., the actual ice thickness of the ice within the grid cell weighted by the sea ice concentration A: $h = h_{\text{actual}}A$. f is the Coriolis parameter, $\mathbf{k}$ is the vertical unit vector, $\boldsymbol{\tau}_a$ and $\boldsymbol{\tau}_o$ are ice-atmosphere and ice-ocean interfacial stresses, g is the gravitational acceleration, $\Delta\,H$ is the gradient of the sea surface height, and $\boldsymbol{\sigma}$ is the (vertically integrated) stress tensor. Nonlinear momentum advection is neglected. The horizontal ice velocity $\mathbf{u} = u\mathbf{i} + v\mathbf{j}$ advects the sea ice thickness h and sea ice concentration A (Losch et al., 2010). Following Lemieux et al. (2015), the basal drag term $\boldsymbol{\tau}_b$ is zero when the ice thickness h is smaller than a critical mean thickness $h_c = A\,h_w/k_1$ where h_w is the water depth. For thicknesses larger than h_c, the basal drag is given by $\boldsymbol{\tau}_b = k_2\frac{\boldsymbol{u}}{|\boldsymbol{u}|+u_0}(h-h_c)\,e^{-C_b(1-A)}$. Here, $C_b = 20$ as for the equivalent formulation of the ice strength (Lemieux et al., 2015), $|\mathbf{u}| = \sqrt{u^2+v^2}$, and u_0 is a small velocity parameter to avoid divisions by zero. k_1 and k_2 are the tuning parameters of the grounding scheme. $\boldsymbol{\tau}_l$ is a new lateral drag term described in the next section.

Two characteristics distinguish landfast ice from drift ice: it is attached to the coast, and it moves very little (Zhai et al., 2021; Mahoney et al., 2007, 2014). We classify sea ice as landfast ice when the biweekly average sea ice drift velocity is below a critical value of $5\times10^{-4}\,\mathrm{m\,s^{-1}}$ (Lemieux et al., 2015). This corresponds to a displacement of approximately 600 meters in two weeks. In addition, landfast ice is assumed to be compact with a SIC larger than 95% to exclude accidentally immobile ice far away from the landfast ice region.

3 Lateral drag parameterization

3.1 Boundary condition

The lateral boundary conditions have a profound influence on the lateral friction at the boundaries (Adcroft & Marshall, 1998). Generally, the lateral boundary conditions for velocity are either no-slip or free-slip, or a mix of both. The no-slip boundary condition assumes that the fluid in direct contact with the boundary has the same velocity as this boundary (Rapp, 2017). Therefore, the tangent flow is zero on the boundary. For a C-grid with staggered velocities, this can be implemented using "ghost points" outside the domain. For example, for the tangential component u of the velocity along a boundary b in the x-direction between grid indices j and $j+1$ we have:

$$u\Big|_b \approx \frac{u_j + u_{j+1}}{2} = 0 \Leftrightarrow u_{j+1} = -u_j. \tag{2}$$

A slip boundary condition assumes a discontinuity in the velocity function (i.e., a relative movement between the fluid and the boundary). For the free-slip boundary condition the tangent shear vanishes on the boundary and the tangent flows remain finite (Rapp, 2017):

$$\frac{\partial u}{\partial y}\Big|_b \approx \frac{u_{j+1} - u_j}{\Delta y} = 0 \Leftrightarrow u_{j+1} = u_j. \tag{3}$$

In the following, we use a simple finite difference discretization model to illustrate the lateral friction on the boundary. Note that MITgcm implements a finite volume discretization, which would complicate the discussion unnecessarily. We assume a constant viscosity coefficient ν and constant grid spacing Δy for the lateral friction term in the y-direction. The lateral friction term (viscosity) along the boundary is a function of the tangential velocity u:

$$\begin{aligned}\partial_y \nu \partial_y u &= \partial_y(\nu \partial_y u)\\ &= \frac{(\nu\partial_y u)|_{j+\frac{1}{2}} - (\nu\partial_y u)|_{j-\frac{1}{2}}}{\Delta y}\\ &= \frac{1}{\Delta y}\left(\nu\frac{u_{j+1} - u_j}{\Delta y} - \nu\frac{u_j - u_{j-1}}{\Delta y}\right).\end{aligned} \tag{4}$$

For the no-slip boundary condition Equation (2), the lateral friction term becomes:

$$\partial_y \nu \partial_y u = -\frac{\nu(u_j - u_{j-1})}{(\Delta y)^2} - \frac{2\nu\, u_j}{(\Delta y)^2}. \tag{5}$$

For the free-slip boundary condition Equation (3), the lateral friction term is:

$$\partial_y \nu \partial_y u = \frac{-\nu(u_j - u_{j-1})}{(\Delta y)^2}. \tag{6}$$

Typically, sea ice models use a no-slip boundary condition to parameterize any unresolved frictional boundary layers. Comparing Equation (5) to Equation (6), the difference between the no-slip and free-slip boundary conditions is $-\frac{2\nu\, u_j}{(\Delta y)^2}$. The key idea of our new parameterization is to replace this term, which in viscous plastic models is a complicated, nonlinear function of ice pressure and ice drift velocities, with an explicit lateral drag. Plausibly, the lateral drag term is a function of the sea ice thickness (or mass), the drift velocity and the shape (i.e., resistance) of the coastline, expressed as a form factor. In its most general form, it can be written as:

$$\boldsymbol{\tau}_l = m\, F\, \mathbf{K}(\mathbf{u}), \tag{7}$$

where F is the form factor and $\mathbf{K}(\mathbf{u})$ is a function of the sea ice drift velocity $\mathbf{u}$. The form factor F depends locally on the length of the coastline and is described in detail in Section 3.2. Different types of $\mathbf{K}(\mathbf{u})$ are discussed in Section 3.3.

3.2 Form factor

The form factor F is determined by the relative location of the ocean and the land within a grid cell. The model topography is interpolated from the International Bathymetric Chart of the Arctic Ocean (IBCAO) topography data (Jakobsson et al., 2012) to a 4.5 km grid and then coarse-grained to a 36 km grid. The grid is regarded as an ocean/land point if ocean/land covers more than half of the model grid (Figure 1a). Here, we discuss two types of form factors in the lateral drag parameterization. The first, F_1, is determined by the coastline resolved by the model grid, and the second, F_2, uses a higher subgrid resolution coastline. As the lateral drag affects only velocities parallel to the coastline, the form factor is considered separately in the x- and y-directions. The lateral drag of one grid cell in the x-direction is affected by the coastline in the y-direction.

The coefficient for u-component of the stress, F_1^u, is zero when the two neighboring model grid cells in the y-direction are both ocean points. F_1^u is one when one of the neighboring cells in the y-direction is a land point. F_1^u is two when both of the neighboring grid cells are land points. The coefficient for the v-component, F_1^v, is determined analogously. The definition for this simple form factor is summarized in Equation (8):

$$F_1^{v/u} = \begin{cases} 0, & \text{in x/y direction no land point} \\ 1, & \text{in x/y direction only one land point} \\ 2. & \text{in x/y direction two land points} \end{cases} \quad (8)$$

The second form factor F_2 involves additional sub-grid scale information provided by a high-resolution coastline data set. We use the 10 m coastline data from Natural Earth 10 m Physical Vectors (`https://www.naturalearthdata.com`). We project the 10 m coastline on the x- and y-direction within each grid cell, integrate projected natural coastline length, and normalize it by the model grid length. The normalized integrals of the 10 m coastline within one grid cell $f_2^u(i,j)$ and $f_2^v(i,j)$ are defined as:

$$f_2^u(i,j) = \frac{\sum_{n=1}^{N} |l_n \cos\theta_n|}{\Delta x_{i,j}} \quad (9)$$

$$f_2^v(i,j) = \frac{\sum_{n=1}^{N} |l_n \sin\theta_n|}{\Delta y_{i,j}}. \quad (10)$$

where $f_2^u(i,j)$ and $f_2^v(i,j)$ are projections of the 10 m coastline in the x- and y-direction normalized by the grid length. l_n is the length of the nth segment of 10 m coastline within one grid cell, θ_n is the angle between the nth 10 m coastline segment and x-axis of the model grid, $\Delta x_{i,j}$, $\Delta y_{i,j}$ are the model grid spacings in the x- and y-direction, and N is the number of 10 m coastline points within one model grid cell.

The form factors $F_2^u(i,j)$, $F_2^v(i,j)$ for $u_{i,j}$, $v_{i,j}$ are determined by f_2^u, f_2^v (Figure 1a):

$$F_2^u(i,j) = \frac{f_2^u(i,j) + f_2^u(i,j+1)}{2} \quad (11)$$

$$F_2^v(i,j) = \frac{f_2^v(i,j) + f_2^v(i+1,j)}{2}. \quad (12)$$

Figures 1b and 1c illustrate the two different form factors for the x-direction in the Kara Sea. Based on the high resolution coastline data, form factor F_2 is generally larger than F_1. Geographic features that are unresolved by our 36 km model grid, such as the Franz-Josef-Land archipelago, also lead to non-zero contributions to F_2, so that these features can exert lateral drag.

3.3 Function $\mathbf{K(u)}$

$\mathbf{K}(\mathbf{u})$ is a function of sea ice velocity. Here we test two different forms. The first form is a quadratic function $\mathbf{K}_1(\mathbf{u}) = C_q|\mathbf{u}|\,\mathbf{u}$ similar to the ocean stress $\boldsymbol{\tau}_o$ and atmosphere stress $\boldsymbol{\tau}_a$. The coefficent C_q has the units m^{-1}. The quadratic function $\mathbf{K}_1(\mathbf{u})$

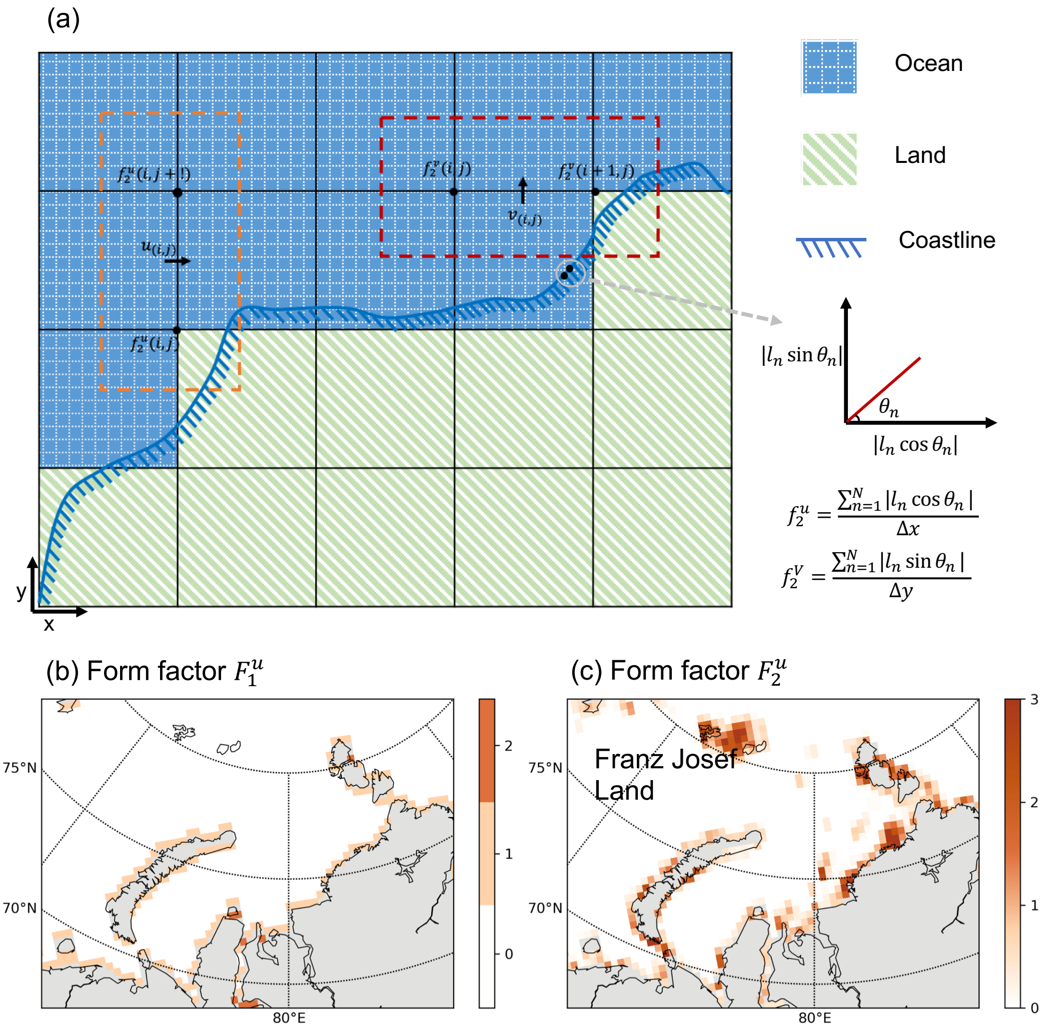

Figure 1. Definition for form factors and two form factors in x-direction in the Kara Sea. (a) Schematic illustration of form factors. The blue line represents the subgrid scale coastline. The grid pattern represents the ocean in the model, and the hashed green area is the land in the 36 km model. $f_2^u(i,j)$ and $f_2^v(i,j)$ are the projections of the subgrid scale coastline in the x- and y-direction normalized by the grid length at the grid (i,j). The point $u_{i,j}$ in the orange box is influenced by the two adjacent points and $F_2^u(i,j)$ is calculated via Equation 11. The point $v_{i,j}$ in the red box is influenced by the two surrounding points and $F_2^v(i,j)$ is defined in Equation 12. (b) and (c): The two form factors in the x-direction in the Kara Sea. Form factor F_1^u assumes values of $0, 1$, and 2. The values of F_2^u are continuous.

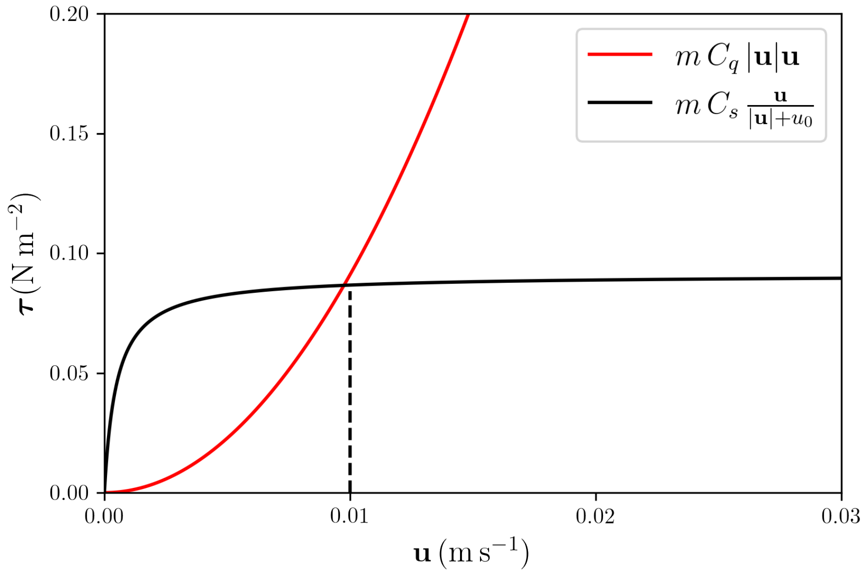

Figure 2. Quadratic and static $\mathbf{K}(\mathbf{u})$ function in the lateral drag parameterization. The red line is the quadratic function $\mathbf{K}_1(\mathbf{u})$ with $C_q = 1\,\mathrm{m^{-1}}$, and the black line indicates the static function of lateral drag with $C_s = 10^{-4}\,\mathrm{m\,s^{-2}}$. $m = \rho_i\,h$ is chosen as $910\,\mathrm{kg\,m^{-2}}$ corresponding to $1\,\mathrm{m}$ of ice. For the static function, the lateral drag increases quickly with sea ice drift below $u_* = 0.01\,\mathrm{m\,s^{-1}}$ (approximately where quadratic and static functions coincide for the chosen parameters) and remains almost constant above. In contrast, $\mathbf{K_1}(\mathbf{u})$ increases quadratically with velocity.

increases with increasing ice velocity (Figure 2). The second form $\mathbf{K}_2(\mathbf{u}) = C_s \frac{1}{|\mathbf{u}|+u_0}\,\mathbf{u}$ is a static friction form similar to the basal drag of Lemieux et al. (2015) with a small velocity $u_0 = 5\times10^{-4}\,\mathrm{m\,s^{-1}}$. The coefficient C_s has the units $\mathrm{m\,s^{-2}}$. The static function $\mathbf{K}_2(\mathbf{u})$ provides constant lateral drag when sea ice drift velocity exceeds the small velocity $u_* = 0.01\,\mathrm{m\,s^{-1}}$ (Figure 2).

The lateral drag parameterization is mainly governed by the function $\mathbf{K}(\mathbf{u})$. To estimate the order of magnitude of lateral drag coefficients, we assume that the lateral drag term has the same order of magnitude as the wind stress term. The order of magnitude of typical wind stress in the Arctic is $0.1\,\mathrm{N\,m^{-2}}$ (Lemieux et al., 2015; Timmermans & Marshall, 2020). To reach a similar magnitude with the wind stress for the lateral drag term, we use a lateral drag coefficient $C_q = 1\,\mathrm{m^{-1}}$ in the quadratic function $\mathbf{K}_1(\mathbf{u})$, and

$C_s = 10^{-4}\,\mathrm{m\,s^{-2}}$ for the static function $\mathbf{K}_2(\mathbf{u})$. With this choice of coefficients the different formulations give similar drag for ice velocities of 0.01 $\mathrm{m\,s^{-1}}$ (Figure 2).

Combining different form factors F and velocity function $\mathbf{K}(\mathbf{u})$, we get four formulations of the lateral drag terms:

$$\boldsymbol{\tau}_{l1} = m\,F_1\,C_q\,|\mathbf{u}|\mathbf{u} \tag{13a}$$

$$\boldsymbol{\tau}_{l2} = m\,F_2\,C_q\,|\mathbf{u}|\mathbf{u} \tag{13b}$$

$$\boldsymbol{\tau}_{l3} = m\,F_1\,C_s\,\frac{\mathbf{u}}{|\mathbf{u}| + u_0} \tag{13c}$$

$$\boldsymbol{\tau}_{l4} = m\,F_2\,C_s\,\frac{\mathbf{u}}{|\mathbf{u}| + u_0} \tag{13d}$$

4 Results

In this section, we compare experiments with different parameterizations to the satellite data of the National Ice Center (NIC) Arctic Sea Ice Charts and Climatologies (U. S. National Ice Center, 2006, updated 2009). To better distinguish the different model simulations, we use the abbreviations for different model simulations provided in Table 1. We first compare four lateral drag formulas, and estimate the sensitivity of the lateral drag coefficient. Next we compare the lateral and basal drag parameterization. Finally, we evaluate the time series of landfast ice extent in four marginal Arctic seas (Kara, Laptev, East Siberian, Beaufort) with satellite observations and assess the large-scale features in the model simulations with the new parameterization. We explicitly exclude landfast ice estimates in the Canadian Arctic Archipelago, as the dynamics there are different and the model generally overestimates the landfast ice cover (Lemieux et al., 2018).

4.1 Landfast ice frequency with different lateral drag formulas

The main aim is to improve the landfast ice representation, in particular in the Kara Sea, because there the water is deeper than in the other marginal seas so that landfast ice cannot form simply due to grounding ice keels. We used the landfast ice frequency in the Kara Sea from January to May in 2001–2007 to compare the four different lateral drag implementations shown in Equation (13). The landfast ice frequency is the frequency of occurrence of landfast ice for January to May in the years 2001–2007. For a

Table 1. The abbreviations of model simulations in this paper.

Abbreviation	Model simulations
CTRL	standard 36 km model control run, no landfast ice parameterization
LD	36 km model with lateral drag parameterization
BD	36 km model with basal drag parameterization
LD + BD	36 km model with both lateral and basal drag parameterization

particular grid cell, a value of 1 means that in each record in the months January to May the ice satisfied the criterion for landfast ice (mean drift < 600 m in 2 weeks) while, a value of 0 means that there was never any landfast ice in this grid cell.

Using the same form factor, the model run with the static function $\mathbf{K}_2(\mathbf{u})$ simulates larger landfast ice frequency in the Kara Sea, which is more consistent with the observations, than that with the quadratic function $\mathbf{K}_1(\mathbf{u})$ (compare Figure 3a with 3c and Figure 3b with 3d). With the same $\mathbf{K}(\mathbf{u})$ function, model simulations with form factor F_2 increases the landfast ice frequency in the Kara Sea compared to simulations with form factor F_1 (compare Figure 3a with 3b and Figure 3c with 3d). This supports the notion that landfast ice in the Kara Sea is mainly supported by sea ice arching as the offshore islands (Severnaya Zemlya archipelago) prevent ice drift and lead to landfast ice formation over the deep regions. The high-resolution coastline underlying the form factor F_2 takes the offshore island chain into account, which leads to higher lateral drag on sea ice.

4.2 Tunning lateral drag parameters

In this section, we test the effects of lateral drag coefficients on simulating landfast ice in the lateral drag parameterization with the static function and form factor F_2. We use timeseries of total landfast ice extent to evaluate different model simulations. The root mean square difference (RMSD) and the mean difference (MD) of landfast ice extent between the model simulations and NIC data are used as metrics. We ran simulations with lateral static drag coefficients, C_s, ranging from $10^{-4}\,\mathrm{m\,s^{-2}}$ to $10^{-3}\,\mathrm{m\,s^{-2}}$. We only show simulations with coefficients 1, 2, 3 $\times\ 10^{-4}\,\mathrm{m\,s^{-2}}$ in Table 2 because these three simulations are closest to observations. We also studied the landfast ice extent in

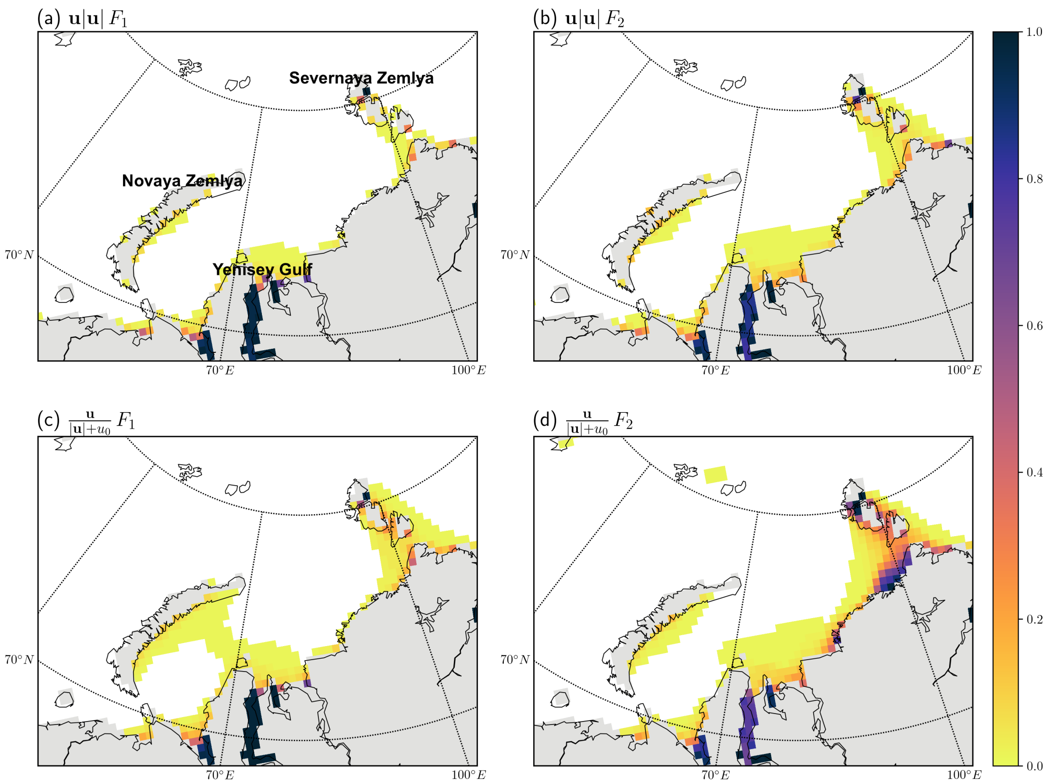

Figure 3. Landfast ice frequency from January to May in 2001–2007 in the Kara Sea with different lateral drag formulations. (a) Quadratic function with simple coast factor F_1 and $C_q = 1\,\mathrm{m^{-1}}$. (b) Quadratic function with normalized coastline length F_2 and $C_q = 1\,\mathrm{m^{-1}}$. (c) Static function with simple coast factor F_1 and $C_s = 1 \times 10^{-4}\,\mathrm{m\,s^{-2}}$. (d) Static function with normalized coastline length F_2 and $C_s = 1 \times 10^{-4}\,\mathrm{m\,s^{-2}}$. The colorbar is the landfast ice frequency, the darker the more often there is landfast ice.

2001–2007 in the Kara Sea in the LD simulations (with lateral drag parameterization) with different lateral drag coefficients (see Figure 4) compared to the CTRL simulation (without any landfast ice parameterizations) and NIC data. The CTRL simulation systematically underestimates landfast ice in the Kara Sea while still capturing the annual and some of the interannual variability (Figure 4). The interannual variability of landfast ice in LD simulations is generally more consistent with observations.

With different lateral drag coefficients the RMSD of landfast ice extent in the Kara Sea does not change much. The LD simulation with lateral drag coefficient $C_s = 2 \times 10^{-4}\,\mathrm{m\,s^{-2}}$ has the smallest RMSD ($5.44{\times}10^4\,\mathrm{km}^2$, about 55% of the RMS of the NIC time series, Table 2). Note that the RMSD in LD simulation with $C_s = 2{\times}10^{-4}\,\mathrm{m\,s^{-2}}$ is not small because of the landfast ice extent outliers in the year 2002 and 2006 in the Kara Sea (see Figure 4). In contrast, the mean differences distinguish LD simulations with different lateral drag coefficients. The LD simulation with a lateral drag coefficient of $C_s = 10^{-4}\,\mathrm{m\,s^{-2}}$ underestimates landfast ice in the Kara Sea ($3.27 \times 10^4\,\mathrm{km}^2$ less than the observation, about 41% of the mean of the NIC time series), whereas $C_s = 3\times 10^{-4}\,\mathrm{m\,s^{-2}}$ leads to an overestimation of landfast ice in the Kara Sea ($1.41 \times 10^4\,\mathrm{km}^2$ larger than the observation, about 18% of the NIC average). The best agreement with the NIC data, with a mean difference of $-0.60 \times 10^4\,\mathrm{km}^2$ (about 8% of the NIC average) in the Kara Sea, is found with $C_s = 2 \times 10^{-4}\,\mathrm{m\,s^{-2}}$ (Table 2).

The large RMSD and mean differences in the Laptev Sea and the East Siberian Sea show that the lateral drag parameterization underestimates landfast ice in these two regions. Because these two regions are exposed to open ocean with no arching from island chains, lateral drag cannot support landfast ice. Instead, the grounding scheme is the primary mechanism to stabilize landfast ice in the Laptev Sea and the East Siberian Sea (Lemieux et al., 2015). However, in the focus of our study, the Kara Sea, the lateral drag parameterization plays a more important role. Consequently, we use lateral drag coefficient $C_s = 2 \times 10^{-4}\,\mathrm{m\,s^{-2}}$ for the further analysis of this paper.

4.3 Comparing effects of lateral and basal drag parameterization on landfast ice extent

We studied the spatial distribution of landfast ice in the Arctic for different combinations of parameterizations for lateral and basal drag (Figure 5). The tuning param-

Table 2. Landfast ice extent statistics of model simulations with different lateral drag coefficients C_s (in $10^{-4}\,\mathrm{m\,s^{-2}}$) with respect to observations in 2001–2007. MD is the mean difference, RMS is the root mean square, and RMSD is the root mean square difference (in $10^4\,\mathrm{km}^2$).

C_s (in $10^{-4}\,\mathrm{m\,s^{-2}}$)	1		2		3		NIC	
	RMSD	MD	RMSD	MD	RMSD	MD	RMS	Mean
Kara Sea	5.64	-3.27	5.44	-0.60	6.64	1.41	9.96	7.93
Laptev Sea	8.95	-6.51	7.68	-5.12	6.92	-4.15	12.70	9.98
East Siberian Sea	10.90	-7.42	10.10	-6.71	9.55	-6.16	13.90	10.0
Beaufort Sea	1.68	-0.61	1.84	-0.14	1.96	0.13	1.93	1.37

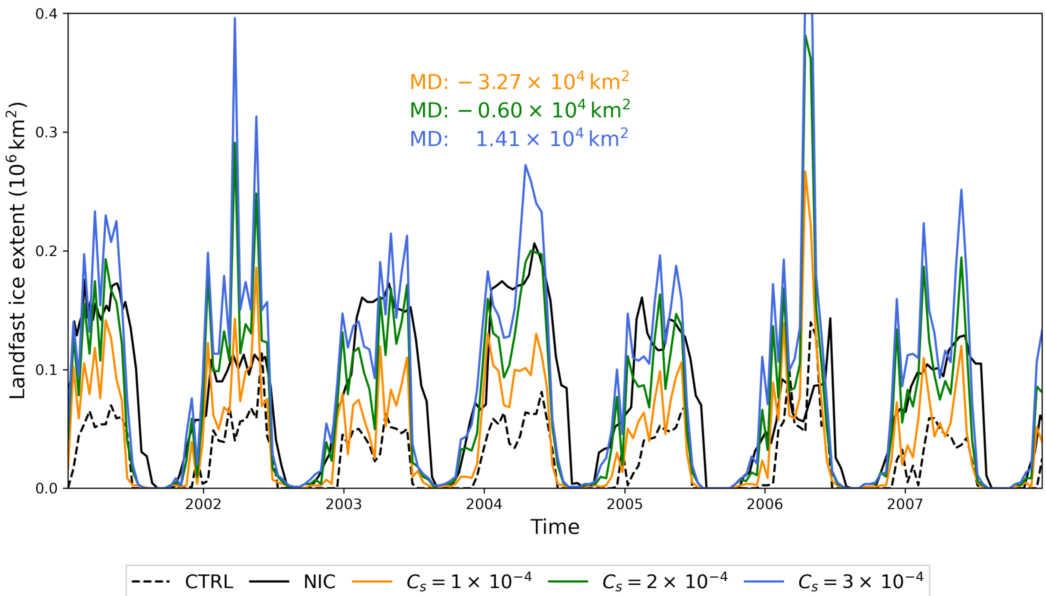

Figure 4. Landfast ice extent in Kara Sea in 2001–2007. Orange, green, and blue lines are the LD experiment with $C_s = 1 \times 10^{-4}\,\mathrm{m\,s^{-2}}$, $C_s = 2 \times 10^{-4}\,\mathrm{m\,s^{-2}}$ and $C_s = 3 \times 10^{-4}\,\mathrm{m\,s^{-2}}$, respectively. The black line is the NIC data, and the black dashed line is the CTRL simulation. The numbers show the mean differences of landfast ice extent in four regions between LDs and observation for the years 2001–2007.

eters of the grounding scheme depend on resolution. From experiments with the grounding scheme for $k_1 = 6, 7, 8, 10$ and $k_2 = 5, 10, 15\,\mathrm{N\,m^{-3}}$ (summarized in Table A1 in the appendix) we find that, consistent with Lemieux et al. (2015), the set $k_1 = 8$, $k_2 = 15\,\mathrm{N\,m^{-3}}$ provides best agreement to the satellite data in the Laptev Sea in our configuration (RMSD=$4.55\times10^4\,\mathrm{km^2}$ and MD $= -1.06\times10^4\,\mathrm{km^2}$), but overestimated landfast ice extent in the East Siberian Sea (RMSD=$7.32\times10^4\,\mathrm{km^2}$ and MD $= 3.44\times10^4\,\mathrm{km^2}$) and the Beaufort Sea (RMSD=$1.70\times10^4\,\mathrm{km^2}$ and MD $= 0.18\times10^4\,\mathrm{km^2}$). Still we use this parameter combination to compare to previous results. Note that the basal drag parameterization underestimates the landfast ice extent in the Kara Sea (RMSD=$4.95\times10^4\,\mathrm{km^2}$ and MD $= -2.91\times10^4\,\mathrm{km^2}$), which is also consistent with Lemieux et al. (2015).

Because landfast ice formation mechanisms are related to topography and geography, we use the Kara Sea (deep region) as the reference region to study the lateral drag parameterization and the Laptev Sea (shallow region) as the reference region for the basal drag parameterization. The Kara Sea is different from the Laptev Sea in topography and water depth, so that the parameterized mechanisms that lead to landfast ice are different and most likely complementary. Therefore, we refrain from retuning all three parameters k_1, k_2, and C_s in the combination run LD+BD (with lateral and basal drag parameterization), but use the parameter values found in the runs LD and BD simulations (with basal drag parameterization).

The lateral drag parameterization improves the representation of landfast ice in the Kara Sea. With only the basal drag parameterization (BD), the landfast ice extent in the Kara Sea is strongly underestimated compared to observations (with a mean difference of $-2.91\times10^4\,\mathrm{km^2}$, about 37% of the NIC average). The LD simulation reduces this difference to $-0.60\times10^4\,\mathrm{km^2}$ (Table 3) and the distribution of relative frequency in the Kara Sea also improves compared to the BD simulation (Figure 5). In the LD + BD simulation, the mean landfast ice extent in the Kara Sea is larger than in the observation by $0.88\times10^4\,\mathrm{km^2}$ (about 11% of the NIC average, Table 3). The Severnaya Zemlya archipelago in the Kara Sea provides anchor points and exerts lateral friction such that more sea ice attaches to the coast. Since the LD simulation contains additional coastline information, there is also some landfast ice in the LD simulation near Franz-Josef-Land archipelago ($\approx 81°$N, $55°$E), an archipelago that is unresolved by the model grid. The larger RMSD ($5.44\times10^4\,\mathrm{km^2}$) can be explained by the short outliers in 2002 and 2006 (see Figure 6b, and Section 5) when the LD simulation overestimates landfast ice

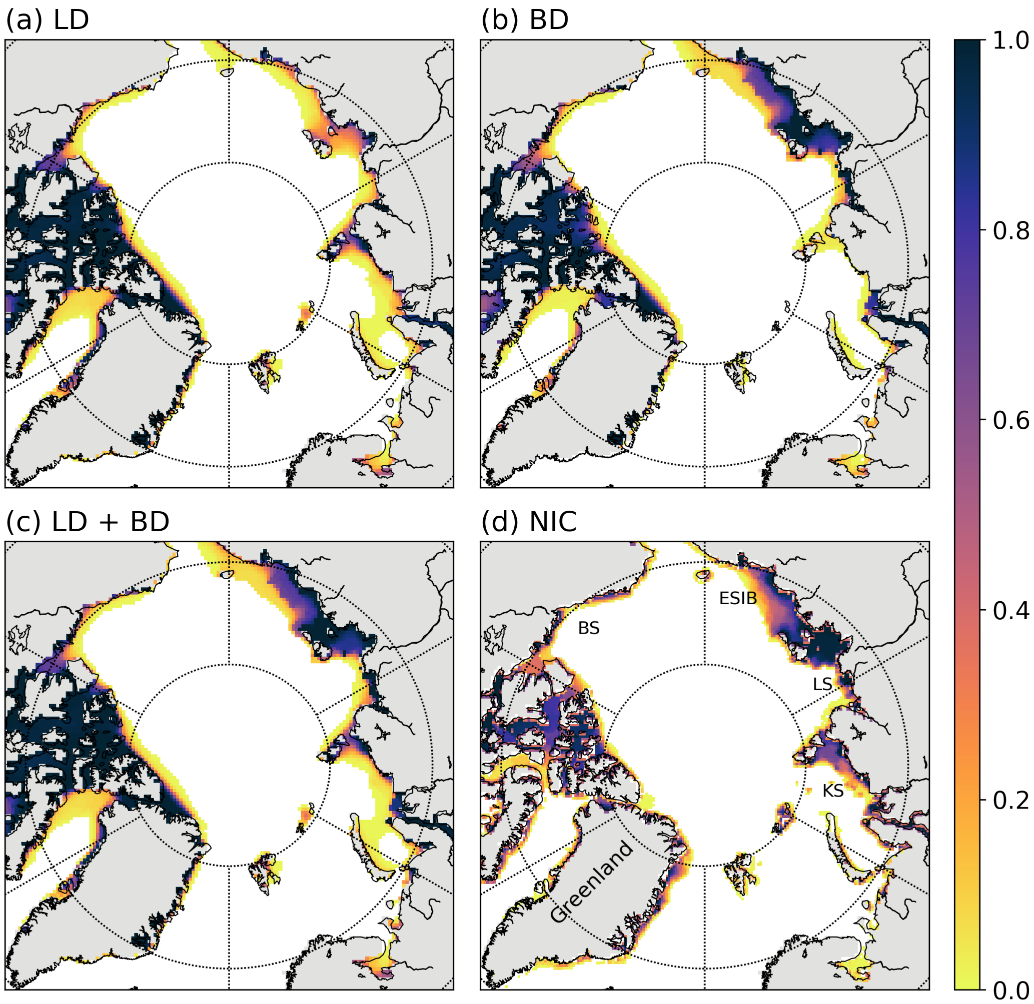

Figure 5. Landfast ice frequency for January to May in 2001–2007 in the Arctic. (a) LD with lateral drag coefficient $C_s = 2 \times 10^{-4}\,\mathrm{m\,s^{-2}}$. (b) BD with basal drag parameters $k_1 = 8$, $k_2 = 15\,\mathrm{N\,m^{-3}}$. The solid and dashed isolines represent the 25 m and the 60 m depth contours. (c) LD + BD with lateral drag coefficient $C_s = 2 \times 10^{-4}\,\mathrm{m\,s^{-2}}$, $k_1 = 8$, $k_2 = 15\,\mathrm{N\,m^{-3}}$. (d) NIC data. BS: Beaufort Sea, ESIB: East Siberian Sea, LS: Laptev Sea, KS: Kara Sea.

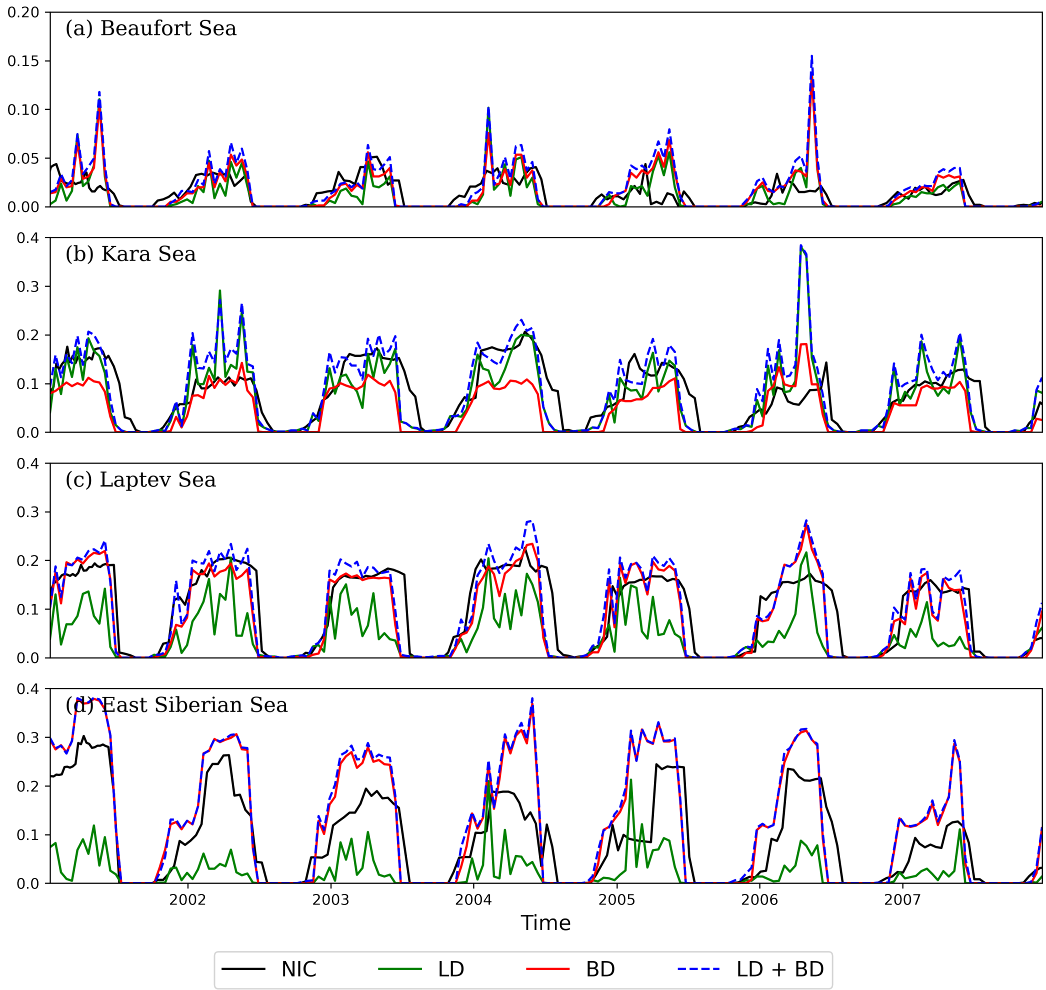

Figure 6. Time series of landfast ice extent ($10^6\,\mathrm{km}^2$) in four regions: (a) the Beaufort Sea; (b) the Kara Sea; (c) the Laptev Sea; and (d) the East Siberian Sea. NIC: observations, LD: lateral drag run, BD: basal drag run, LD + BD: run with both lateral and basal drag parameterization.

in the Western Kara Sea near Novaya Zemlya. Note that the two peaks in the LD simulation two weeks before March 24, 2002 and April 16, 2006 also appear in the model simulations with grounding scheme (see Figure 6b and Lemieux et al. (2015), their Figure 6b). The BD simulation underestimates the landfast ice extent in the Kara Sea, but improves it near the Yenisey Gulf compared to the LD simulation (Figure 5b), because the scheme successfully parameterizes the grounding pressure ridges in this shallow region (McClelland et al., 2012; Harms, 2004).

Table 3. Landfast ice statistics of different model simulations with respect to observations in 2001–2007 (in $10^4\,\mathrm{km}^2$). RMSD: root mean square difference, MD: mean difference, LD: lateral drag run, BD: basal drag run, LD + BD: run with both lateral and basal drag parameterization.

Regions	LD		BD		LD + BD	
	RMSD	MD	RMSD	MD	RMSD	MD
Kara Sea	5.44	-0.60	4.95	-2.91	5.61	0.88
Laptev Sea	7.68	-5.12	4.55	-1.06	4.64	-0.05
East Siberian Sea	10.10	-6.71	7.32	3.44	7.63	3.82
Beaufort Sea	1.84	-0.14	1.70	0.18	2.05	0.49

The basal drag parameterization increases the landfast ice formation in the Laptev Sea (see also Lemieux et al., 2015, 2016). The mean landfast ice extent in the Laptev Sea in the LD + BD simulation is on average $0.05\times10^4\,\mathrm{km}^2$ smaller than the observation (about 0.5% of the mean of the NIC time series, Table 3). Combining the lateral and basal drag parameterizations reduces the mean differences compared to lateral drag or basal drag parameterization alone in the Laptev Sea. Landfast ice ridges reach the bottom in the Laptev Sea to sustain sea ice attached to the coast. Coastlines also provide anchor points for landfast ice when ice floes drift onshore.

In the East Siberian and Beaufort seas, the additional effect of the lateral drag parameterization leads to an overestimation of landfast ice extent so that the mean differences of landfast ice extent in LD + BD simulation in the East Siberian Sea and the Beaufort Sea ($3.82\times10^4\,\mathrm{km}^2$ and $0.49\times10^4\,\mathrm{km}^2$) are slightly larger than that in the simulation only using basal drag (BD) parameterization. On average, the combination of lateral and basal drag improves the landfast ice simulations in all Arctic marginal seas.

4.4 Comparison of large scale features between CTRL and LD simulation

In this section we examine the sea ice concentration (SIC) and sea ice thickness (SIT) in the model simulations with lateral drag parameterization in April 2001–2007. Compared to the CTRL simulation, SIC in the LD simulation differs in the marginal ice zone (MIZ), while SIT differences are very small. In landfast ice regions, SIT is slightly thinner and everywhere else it is slightly thicker (<10 cm) than in the CTRL simulation (not shown). As expected, the lateral drag parameterization does not directly influence regions far away from the coast.

In the following we use ice thickness data from the Panarctic Ice Ocean Modeling and Assimilation System (PIOMAS, Schweiger et al., 2011; Zhang & Rothrock, 2003) as a rough reference for our simulations to evaluate the effect of the new parameterization on the net ice volume in the Arctic. The PIOMAS volume timeseries has a mean annual cycle of $21.2\times10^3\,\mathrm{km}^3$ and an RMS of $19.3\times10^3\,\mathrm{km}^3$. The RMSD between the time series of Arctic sea ice volume in 2001–2007 between PIOMAS and our LD simulation (Figure 7) is $5.44\times10^3\,\mathrm{km}^3$ (about 28% of the RMS of the sea ice volume in PIOMAS). The RMSD between the LD simulation and our CTRL simulation is more than a factor of 10 smaller: $0.47\times10^3\,\mathrm{km}^3$ (about 2% of the RMS of the sea ice volume in PIOMAS). PIOMAS uses a special teardrop rheology that allows biaxial tensile stress (Zhang & Rothrock, 2005). In this sense, it implicitly allows landfast ice similar to the tensile strength approach with an elliptical yield curve in Lemieux et al. (2016). PIOMAS does not use any other explicit parameterization scheme for landfast ice (J. Zhang, personal communications), but our results suggest that the difference in Arctic-wide mean thickness of such a scheme would be small. The LD (and LD+BD) simulation leads to a very similar sea ice volume and extent compared to the CTRL simulation. The RMSD of sea ice extent between LD simulations and estimates of the Arctic Data archive System (ADS) Quasi-real-time polar environment observation monitor (Yabuki et al., 2011) is $1.35\times10^6\,\mathrm{km}^2$. The RMSD of sea ice extent between the LD simulation and the CTRL simulation is $0.06\times10^6\,\mathrm{km}^2$. Generally, the lateral drag parameterization slightly decreases the mean ice volume by 1.9% compared to the CTRL simulation, mainly through thinner ice in the landfast ice areas, but otherwise has little effect on the large scale properties of the solution.

5 Discussion

The results presented in Section 4 demonstrate that the mechanism for landfast ice formation largely depends on geography. Grounding of ice keels is the dominant mechanism to form landfast ice in regions shallower than a critical depth. In contrast, lateral drag is more important in regions exceeding the critical water depth, where island chains provide pinning points for sea ice arches. However, the lateral drag parameterization cannot replace, but can only augment the grounding scheme because by itself it produces

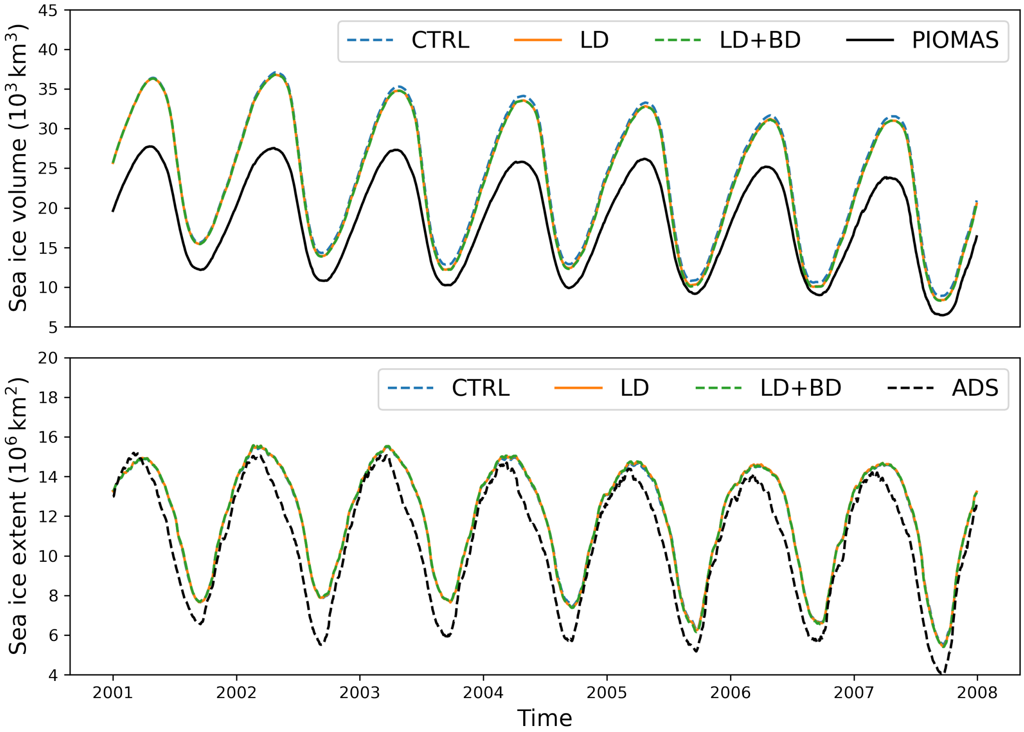

Figure 7. Time series of sea ice volume and sea ice extent over the arctic in 2001–2007. The reference data for sea ice volume and sea ice extent is from PIOMAS and ADS, respectively.

too little landfast ice in the shallow regions; i.e., the Laptev Sea and the East Siberian Sea where there are no islands to act as anchor points. Both physical processes should be parameterized concurrently to simulate landfast ice in the entire Arctic.

The lateral drag parameterization improves the landfast ice simulation in the Kara Sea, but it overestimates landfast ice in the Western Kara Sea in March 2002 and April 2006. We investigated one-week averaged wind velocity and sea ice thickness before March 24, 2002 and April 16, 2006 to explore potential reasons for the overestimation of landfast ice. Two time periods for the same date in 2005 and 2007 were also picked for comparison. Here we provide two hypotheses to explain this phenomenon. One of the hypotheses is related to the wind direction leading to the anomalous landfast ice. When the wind blows perpendicular to Novaya Zemlya, there is excessive landfast ice in the Western Kara Sea. Sea ice piles up in the Western Kara Sea, attaches to the coast, and becomes landfast ice (see Figure 8a, 8b). However, when the wind blows parallel to the coast, there is no landfast ice in the Western Kara Sea (Figure 8d). The second hypothesis is a combination of local wind patterns and landfast ice diagnostics artifacts. During the observed periods of high landfast ice in the Western Kara Sea in 2002 and 2006, there were anticyclonic wind patterns around the Kara Sea, which may have led to Ekman convergence, where the ice is not moved away but "pushed together" in convergence (Figure 8b). As a consequence, the immobile sea ice is falsely diagnosed as landfast ice. These processes may also lead to the higher temporal variability in landfast ice compared to observations (see Figure 6). A similar process reduces sea ice speed, albeit at larger scales in the Beaufort Sea, when ice concentration and internal stresses are high in wintertime during an anticyclonic anomaly (Wang et al., 2019). As a test, we calculate the landfast ice frequency in the Kara Sea from January to May in 2001–2007, excluding March 2002 and April 2006. The results show a close agreement with the NIC data for the simulations with lateral drag parameterization alone and the combination of lateral drag parameterization and grounding scheme in the Kara Sea (Figure 9).

Attempts to improve landfast ice simulation in the Kara Sea by modifying global parameters in the sea ice model (e.g., implementing a large maximum viscosity in a regional sea ice model (Olason, 2016), or adding tensile strength to the rheology (Beatty & Holland, 2010; Lemieux et al., 2016)) were successful. However, they have the disadvantage that they affect the sea ice dynamics in the entire Arctic. In contrast, the approaches based on domain geometry such as the depth-dependent grounding scheme or

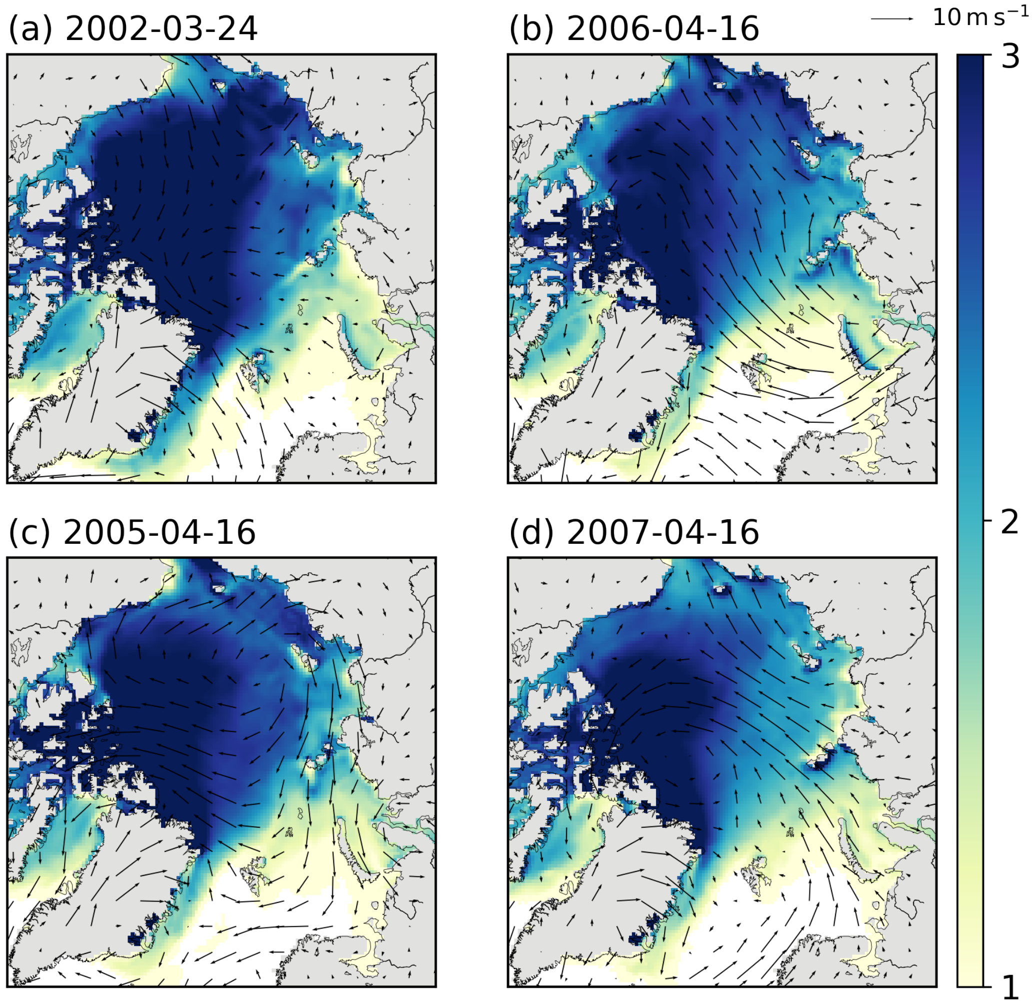

Figure 8. One week average of sea ice thickness (m) and wind velocity (m s^{-1}) before: (a) 24 March 2002 (high landfast ice); (b) 16 April 2006 (high landfast ice); (c) 16 April 2005 (for reference); (d) 16 April 2007 (for reference). The colorbar describes the sea ice thickness (m), the wind velocity reference is 10 m s^{-1}.

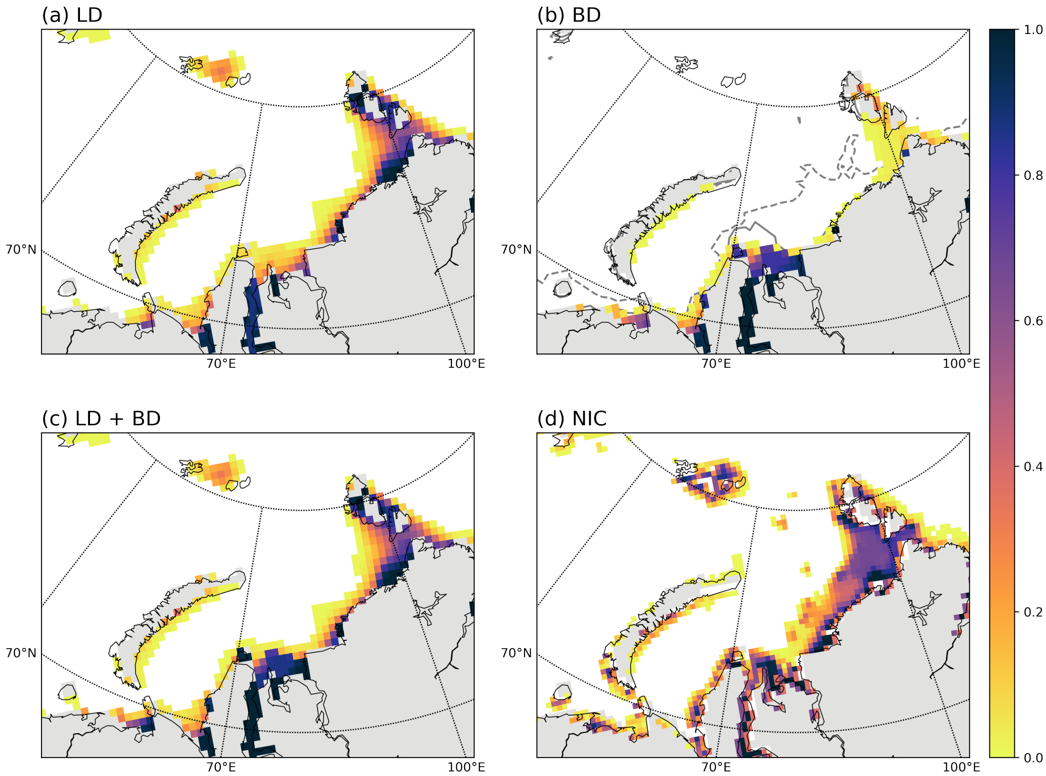

Figure 9. Landfast ice frequency for January to May in 2001–2007 in the Kara Sea with data in the two weeks with exceptionally large landfast ice in 2002 and 2006 excluded. The solid and dashed isolines in (b) represent the 25 m and the 60 m depth contours in the Kara Sea.

our new lateral drag scheme along coastlines affect the pan-Arctic scale far away from the coasts only indirectly. The form factor in the lateral drag parameterization allows including additional subgrid information independent of model resolution. This extra information leads to realistic effects of unresolved coastline in the coarse model.

Landfast ice in Antarctica is often attached to grounded icebergs which ground in water depth of 400-500 m, or to other coastal features (e.g., the shoreline, glacier tongues, and ice shelves, Massom et al., 2001; Fraser et al., 2012, 2020). Because of the deep continental shelves around Antarctica, the grounding scheme may not work as well as in the Arctic. Including our lateral drag parameterization in an Antarctic sea ice model may lead to realistic landfast ice simulations.

Implementing a lateral drag parameterization is very simple and improves landfast ice estimates in the deep regions in the Arctic; therefore, we recommend including it for any sea ice model. The only complication is that, strictly speaking, the lateral no-slip boundary condition needs to be replaced by a free-slip condition, in order not to add two types of lateral drag. We found that the additional information on high-resolution coastlines is important because it adds drag to the model also where archipelagos are not resolved by the model grid.

Explicit landfast ice thickness observations are rare because usually they are very localized in-situ point measurements. In our model simulations, we can explore the landfast ice thickness with or without landfast ice parameterizations. We find that the maximum of the mean landfast ice thickness increases from about 0.25 m in the CTRL simulation (without explicit landfast ice parameterization) to about 1 m in the Kara and Beaufort seas, 1.5 m in the Laptev Sea, and 2 m in the East Siberian Sea in simulations with lateral and basal drag parameterization. These numbers can be compared to singular studies such as Zhai et al. (2021) who used a thermodynamic model for the coast of Kotely Island in the East Siberian Sea to simulate landfast ice thickness. They found maximum landfast ice thicknesses 2.02 ± 0.12 m for the years 1994 to 2014. These numbers coincide with our simulations, but since the complicated thermodynamic column model of Zhai et al. (2021) is very different from our fully coupled sea ice-ocean model with very simple thermodynamics, this coincidence should be seen as fortuitous. Note the positive feedback between landfast ice thickness and lateral drag parameterization, where thicker ice leads to a larger lateral drag in the momentum equations.

Our model does not include tides that would be necessary to implement parameterization of landfast ice break-up in the Canadian Arctic Archipelago (Lemieux et al., 2018). Typically, sea ice model overestimates landfast ice extent and duration because the ice is landlocked and the channel in the CAA is not properly resolved. Strong tidal currents can reduce the extent of landfast ice. Adding a landfast ice parameterization that aims to increase the landfast ice extent (no matter if lateral or basal drag parameterization) increases the overestimation of landfast ice in the Canadian Arctic Archipelago. Tides are also reported to be responsible for the reduction of sea ice volume by enhanced vertical mixing (Janout & Lenn, 2014; Luneva et al., 2015). Although strong internal tides are propagating from the Kara Strait to the Barents Sea (Morozov et al., 2008), the tidal currents in the northeastern Kara Sea (Padman & Erofeeva, 2004) and the northern Laptev Sea (Pnyushkov & Polyakov, 2012) are weak. The weak tides are unlikely to decrease the landfast ice cover in the northeastern Kara Sea, but tidal forcing may have a small effect on the landfast ice in the southwestern Kara Sea when only little landfast ice has been formed there.

6 Conclusion

This paper introduces a lateral drag parameterization to improve landfast ice simulation in the Arctic region. The lateral drag parameterization replaces the common no-slip boundary condition in the sea ice momentum equation by a lateral drag term, which is a function of sea ice velocity, and coastline features. We assume that lateral friction is a static function of sea ice velocity and generate a form factor to represent the complexity of the coastline. Numerical experiments were conducted with an Arctic sea ice-ocean model with a grid spacing of 36 km. The landfast ice extent and frequency of model simulations with lateral drag parameterization and grounding schemes were examined in four regions: the Kara Sea, the Laptev Sea, the East Siberian Sea, and the Beaufort Sea. Compared to no parameterization and grounding scheme, lateral drag parametrization leads to a more realistic landfast ice area in the Kara Sea. Although lateral drag parameterization successfully simulates landfast in the Kara Sea, it underestimates landfast ice in the East Siberian Sea, Laptev, and the Beaufort Sea compared to the grounding scheme, because the mechanism of landfast ice formation is different in these regions. The combination of lateral and basal drag parameterization leads to the most realistic estimates of landfast ice in space and time and captures most of the annual cycle and the interannual variability in the Arctic. Thus, we recommend using the lateral and basal drag parameterization in combination to simulate landfast ice in the Arctic Ocean accurately.

In Antarctica, landfast ice forms dynamically when sea ice is imported by onshore winds and blocked by restrictive geometry, for example, the icebergs in deep water (Massom et al., 2001; Van Achter et al., 2022). The lateral drag parameterization provides a way to quantify the mechanism to sustain landfast ice along icebergs, similar to the way coastlines or islands provide anchor points for landfast ice in the Arctic.

Landfast ice limits dynamical thickness growth by preventing rapid ice compression in convergent motion (Itkin et al., 2015). In our simulations, the mean sea ice volume in the Arctic (thickness) in April decreased by around 1.9% after adding a landfast ice parameterization. In the marginal seas, the landfast ice parameterization increases the landfast ice thickness in the Arctic in our simulations, which is most likely an improvement over too little and too thin landfast ice. The simulated landfast ice thickness is also consistent with previous work on landfast ice thickness in the East Siberian Sea (Zhai et al., 2021), giving us confidence that appropriate landfast ice parameterization in the sea ice models will make improved projections for landfast ice distribution and thickness in the Arctic possible.

Once a stable landfast ice cover has developed, new ice formation is reduced on the shelf and especially along the coast; thus, less brine is released into the ocean leading to a fresher upper ocean in landfast ice-covered regions (Itkin et al., 2015). We speculate that the lower salinity in the Kara Sea due to more landfast ice is transported to the Makarov Basin via the Vilkitsky Strait (Janout et al., 2015), which suggests that the landfast ice parameterization may influence the hydrography in the central Arctic. The effects of more realistic landfast ice simulations in the Kara Sea are the subject of future research.

Acknowledgments

The authors thank Bruno Tremblay for the suggestions of the static friction form of the form factor in the paper and Damien Ringeisen for writing suggestions. This work is supported under DFG-funded International Research Training Group ArcTrain (IRTG 1904 ArcTrain). We thank reviewer Bin Cheng and editor Laurence Padman for critically reading the manuscript and suggesting substantial improvements and helpful comments.

Code availability. The code of the lateral drag parameterization in the MITgcm is available at `https://github.com/yqliu11/MITgcm/tree/seaice_lateraldrag_v3`.

Data availability: the satellite data used in this publication are available at

- Landfast ice data: U.S. National Ice Center Arctic Sea Ice Charts and Climatologies in Gridded Format, 1972–2007, Version 1: `https://nsidc.org/data/G02172`
- Sea ice extent via Arctic data archive system: `https://ads.nipr.ac.jp/`
- Sea ice volume data via PIOMAS: `http://psc.apl.uw.edu/research/projects/arctic-sea-ice-volume-anomaly/data/`

Appendix A Table of statistics of BD model simulations

References

Adcroft, A., & Marshall, D. (1998). How slippery are piecewise-constant coastlines in numerical ocean models? *Tellus, Ser. A Dyn. Meteorol. Oceanogr.*, *50*(1), 95–108. doi: 10.3402/tellusa.v50i1.14514

Beatty, C. K., & Holland, D. M. (2010). Modeling landfast sea ice by adding tensile strength. *J. Phys. Oceanogr.*, *40*(1), 185–198. doi: 10.1175/2009JPO4105.1

Dee, D. P., Uppala, S. M., Simmons, A. J., Berrisford, P., Poli, P., Kobayashi, S., ... Vitart, F. (2011). The ERA-Interim reanalysis: Configuration and performance of the data assimilation system. *Q. J. R. Meteorol. Soc.*, *137*(656), 553–597. doi: 10.1002/qj.828

Divine, D. V., Korsnes, R., Makshtas, A. P., Godtliebsen, F., & Svendsen, H. (2005). Atmospheric-driven state transfer of shore-fast ice in the northeastern Kara Sea. *J. Geophys. Res. C Ocean.*, *110*(9), 1–13. doi: 10.1029/2004JC002706

Eicken, H., Dmitrenko, I., Tyshko, K., Darovskikh, A., Dierking, W., Blahak, U., ... Kassens, H. (2005). Zonation of the Laptev Sea landfast ice cover and its importance in a frozen estuary. *Glob. Planet. Change*, *48*(1-3 SPEC. ISS.), 55–83. doi: 10.1016/j.gloplacha.2004.12.005

Flato, G. M., & Brown, R. D. (1996, nov). Variability and climate sensitivity of landfast Arctic sea ice. *J. Geophys. Res. Ocean.*, *101*(C11), 25767–25777. doi:

Table A1. RMSD of model simulations with basal drag parameterization with respect to observations in 2001–2007 in four marginal seas (10^4 km^2).

	RMSD				MD			
	Kara Sea	Laptev Sea	East Siberian Sea	Beaufort Sea	Kara Sea	Laptev Sea	East Siberian Sea	Beaufort Sea
$k_1 = 6, k_2 = 5$	6.16	6.21	5.20	1.64	-4.35	-3.76	-1.56	-0.24
$k_1 = 6, k_2 = 10$	5.97	5.96	5.25	1.65	-4.15	-3.44	-1.24	-0.19
$k_1 = 6, k_2 = 15$	5.88	5.88	5.29	1.65	-4.04	-3.33	-1.09	-0.17
$k_1 = 7, k_2 = 5$	5.57	5.52	5.37	1.66	-3.75	-2.93	0.58	-0.09
$k_1 = 7, k_2 = 10$	5.34	5.29	5.65	1.64	-3.55	-2.6	1.23	-0.02
$k_1 = 7, k_2 = 15$	5.23	5.17	5.79	1.66	-3.4	-2.44	1.54	0.02
$k_1 = 8, k_2 = 5$	5.13	4.79	6.43	1.68	-3.27	-1.9	2.50	0.08
$k_1 = 8, k_2 = 10$	5.02	4.63	7.06	1.68	-3.03	-1.46	3.15	0.14
$k_1 = 8, k_2 = 15$	4.95	4.55	7.32	1.70	-2.91	-1.06	3.44	0.18
$k_1 = 10, k_2 = 5$	4.86	5.27	9.75	1.76	-2.51	0.82	5.53	0.34
$k_1 = 10, k_2 = 10$	4.71	5.63	10.60	1.77	-2.17	1.40	6.40	0.39
$k_1 = 10, k_2 = 15$	9.55	12.30	12.60	1.84	-7.48	-9.51	-8.89	-1.28

10.1029/96JC02431

Fraser, A. D., Massom, R. A., Michael, K. J., Galton-Fenzi, B. K., & Lieser, J. L. (2012). East Antarctic landfast sea ice distribution and variability, 2000–08. *J. Clim.*, *25*(4), 1137–1156. doi: 10.1175/JCLI-D-10-05032.1

Fraser, A. D., Massom, R. A., Ohshima, K. I., Willmes, S., Kappes, P. J., Cartwright, J., & Porter-Smith, R. (2020). High-resolution mapping of circum-Antarctic landfast sea ice distribution, 2000-2018. *Earth Syst. Sci. Data*, *12*(4), 2987–2999. doi: 10.5194/essd-12-2987-2020

Greene, C. A., Young, D. A., Gwyther, D. E., Galton-Fenzi, B. K., & Blankenship, D. D. (2018). Seasonal dynamics of Totten Ice Shelf controlled by sea ice buttressing. *Cryosphere*, *12*(9), 2869–2882. Retrieved from `https://tc.copernicus.org/articles/12/2869/2018/` doi: 10.5194/tc-12-2869-2018

Harms, I. (2004). *Polar seas oceanography: An integrated case study of the Kara Sea* (Vol. 85) (No. 8). London, U. K: Springer. doi: 10.1029/2004eo080011

Hibler, W. D. (1979). A dynamic thermodynamic sea ice model. *J. Phys. Oceanogr.*, *9*(4), 815–846. doi: 10.1175/1520-0485(1979)009⟨0815:ADTSIM⟩2.0.CO;2

Howell, S. E., Laliberté, F., Kwok, R., Derksen, C., & King, J. (2016). Landfast ice thickness in the Canadian Arctic Archipelago from observations and models. *Cryosphere*, *10*(4), 1463–1475. doi: 10.5194/tc-10-1463-2016

Hughes, N. E., Wilkinson, J. P., & Wadhams, P. (2011). Multi-satellite sensor analysis of fast-ice development in the Norske Øer Ice Barrier, northeast Greenland. *Ann. Glaciol.*, *52*(57 PART 1), 151–160. doi: 10.3189/172756411795931633

Itkin, P., Losch, M., & Gerdes, R. (2015). Landfast ice affects the stability of the Arctic halocline: Evidence from a numerical model. *J. Geophys. Res. Ocean.*, *120*(4), 2622–2635. doi: 10.1002/2014JC010353

Jakobsson, M., Mayer, L., Coakley, B., Dowdeswell, J. A., Forbes, S., Fridman, B., … Weatherall, P. (2012). The International Bathymetric Chart of the Arctic Ocean (IBCAO) Version 3.0. *Geophys. Res. Lett.*, *39*(12), 1–6. doi: 10.1029/2012GL052219

Janout, M. A., Aksenov, Y., Hölemann, J. A., Rabe, B., Schauer, U., Polyakov, I. V., … Timokhov, L. (2015). Kara Sea freshwater transport through Vilkitsky Strait: Variability, forcing, and further pathways toward the western

Arctic Ocean from a model and observations. *J. Geophys. Res. Ocean.*, *120*(7), 4925–4944. doi: 10.1002/2014JC010635

Janout, M. A., & Lenn, Y.-D. (2014). Semidiurnal Tides on the Laptev Sea Shelf with Implications for Shear and Vertical Mixing. *J. Phys. Oceanogr.*, *44*(1), 202–219. doi: 10.1175/JPO-D-12-0240.1

Johnson, M., Proshutinsky, A., Aksenov, Y., Nguyen, A. T., Lindsay, R., Haas, C., . . . De Cuevas, B. (2012). Evaluation of Arctic sea ice thickness simulated by Arctic Ocean model intercomparison project models. *J. Geophys. Res. Ocean.*, *117*(3). doi: 10.1029/2011JC007257

Kooyman, G. L., & Ponganis, P. J. (2014). Chick production at the largest emperor penguin colony decreases by 50% from 2008-10. *Antarct. Sci.*, *26*(1), 33–37. doi: 10.1017/S0954102013000515

Kwok, R. (2018, oct). Arctic sea ice thickness, volume, and multiyear ice coverage: Losses and coupled variability (1958-2018). *Environ. Res. Lett.*, *13*(10), 105005. doi: 10.1088/1748-9326/aae3ec

Lemieux, J. F., Dupont, F., Blain, P., Roy, F., Smith, G. C., & Flato, G. M. (2016). Improving the simulation of landfast ice by combining tensile strength and a parameterization for grounded ridges. *J. Geophys. Res. Ocean.*, *121*(10), 7354–7368. doi: 10.1002/2016JC012006

Lemieux, J. F., Lei, J., Dupont, F., Roy, F., Losch, M., Lique, C., & Laliberté, F. (2018). The impact of tides on simulated landfast ice in a pan-Arctic ice-ocean model. *J. Geophys. Res. Ocean.*, *123*(11), 7747–7762. doi: 10.1029/2018JC014080

Lemieux, J. F., Tremblay, L. B., Dupont, F., Plante, M., Smith, G. C., & Dumont, D. (2015). A basal stress parameterization for modeling landfast ice. *J. Geophys. Res. Ocean.*, *120*(4), 3157–3173. doi: 10.1002/2014JC010678

Leppäranta, M. (2013). Land–ice interaction in the Baltic Sea. *Est. J. Earth Sci.*, *62*(1), 2. doi: 10.3176/earth.2013.01

Li, Z., Zhao, J., Su, J., Li, C., Cheng, B., Hui, F., . . . Shi, L. (2020). Spatial and temporal variations in the extent and thickness of arctic landfast ice. *Remote Sens.*, *12*(1), 64. doi: 10.3390/RS12010064

Losch, M., Menemenlis, D., Campin, J. M., Heimbach, P., & Hill, C. (2010). On the formulation of sea-ice models. Part 1: Effects of different solver implementations and parameterizations. *Ocean Model.*, *33*(1-2), 129–144. doi: 10.1016/j.ocemod.2009.12.008

Luneva, M. V., Aksenov, Y., Harle, J. D., & Holt, J. T. (2015). The effects of tides on the water mass mixing and sea ice in the Arctic Ocean. *J. Geophys. Res. Ocean.*, *120*(10), 6669–6699. doi: 10.1002/2014JC010310

Mahoney, A. R., Eicken, H., Gaylord, A. G., & Gens, R. (2014). Landfast sea ice extent in the Chukchi and Beaufort Seas: The annual cycle and decadal variability. *Cold Reg. Sci. Technol.*, *103*, 41–56. doi: 10.1016/j.coldregions.2014.03.003

Mahoney, A. R., Eicken, H., Gaylord, A. G., & Shapiro, L. (2007). Alaska landfast sea ice: Links with bathymetry and atmospheric circulation. *J. Geophys. Res. Ocean.*, *112*(2). doi: 10.1029/2006JC003559

Marshall, J., Adcroft, A., Hill, C., Perelman, L., & Heisey, C. (1997). A finite-volume, incompressible navier stokes model for, studies of the ocean on parallel computers. *J. Geophys. Res. C Ocean.*, *102*(C3), 5753–5766. doi: 10.1029/96JC02775

Massom, R. A., Hill, K. L., Lytle, V. I., Worby, A. P., Paget, M. J., & Allison, I. (2001). Effects of regional fast-ice and iceberg distributions on the behaviour of the Mertz Glacier polynya, East Antarctica. *Ann. Glaciol.*, *33*, 391–398. doi: 10.3189/172756401781818518

Massom, R. A., Scambos, T. A., Bennetts, L. G., Reid, P., Squire, V. A., & Stammerjohn, S. E. (2018). Antarctic ice shelf disintegration triggered by sea ice loss and ocean swell. *Nature*, *558*(7710), 383–389. doi: 10.1038/s41586-018-0212-1

Massom, R. A., & Stammerjohn, S. E. (2010). Antarctic sea ice change and variability - Physical and ecological implications. *Polar Sci.*, *4*(2), 149–186. doi: 10.1016/j.polar.2010.05.001

McClelland, J. W., Holmes, R. M., Dunton, K. H., & Macdonald, R. W. (2012). *The Arctic Ocean Estuary* (Vol. 35) (No. 2). doi: 10.1007/s12237-010-9357-3

Melling, H. (2002). Sea ice of the northern Canadian Arctic Archipelago. *J. Geophys. Res. Ocean.*, *107*(11). doi: 10.1029/2001jc001102

MITgcm Group. (2009). *MITgcm User Manual.* Cambridge, MA 02139, USA. Retrieved from `https://mitgcm.readthedocs.io/`

Morozov, E. G., Paka, V. T., & Bakhanov, V. V. (2008). Strong internal tides in the Kara Gates Strait. *Geophys. Res. Lett.*, *35*(16). doi: 10.1029/2008GL033804

Olason, E. (2016). A dynamical model of Kara Sea land-fast ice. *J. Geophys. Res. Ocean.*, *121*(5), 3141–3158. doi: 10.1002/2016JC011638

Padman, L., & Erofeeva, S. (2004). A barotropic inverse tidal model for the Arctic Ocean. *Geophys. Res. Lett.*, *31*(2), 2–5. doi: 10.1029/2003GL019003

Pnyushkov, A. V., & Polyakov, I. V. (2012). Observations of tidally induced currents over the continental slope of the Laptev Sea, Arctic Ocean. *J. Phys. Oceanogr.*, *42*(1), 78–94. doi: 10.1175/JPO-D-11-064.1

Rapp, B. E. (2017). *Microfluidics: Modelling, mechanics and mathematics.* Elsevier. doi: 10.1016/C2012-0-02230-2

Schweiger, A., Lindsay, R., Zhang, J., Steele, M., Stern, H., & Kwok, R. (2011). Uncertainty in modeled Arctic sea ice volume. *J. Geophys. Res. Ocean.*, *116*(9), C00D06. doi: 10.1029/2011JC007084

Selyuzhenok, V., Krumpen, T., Mahoney, A., Janout, M., & Gerdes, R. (2015). Seasonal and interannual variability of fast ice extent in the southeastern Laptev Sea between 1999 and 2013. *J. Geophys. Res. Ocean.*, *120*(12), 7791–7806. doi: 10.1002/2015JC011135

Steele, M., Morley, R., & Ermold, W. (2001). PHC: A global ocean hydrography with a high-quality Arctic Ocean. *J. Clim.*, *14*(9), 2079–2087. doi: 10.1175/1520-0442(2001)014⟨2079:PAGOHW⟩2.0.CO;2

Timmermans, M. L., & Marshall, J. (2020). Understanding Arctic Ocean circulation: A review of ocean dynamics in a changing climate. *J. Geophys. Res. Ocean.*, *125*(4). doi: 10.1029/2018JC014378

U. S. National Ice Center. (2006, updated 2009). *U.S. National Ice Center Arctic sea ice charts and climatologies in gridded format, 1972 - 2007, Version 1.* (Tech. Rep.). NSIDC: National Snow and Ice Data Center. Retrieved from `https://doi.org/10.7265/N5X34VDB` (Edited and compiled by Fetterer, F. and Fowler, C.)

Ungermann, M., & Losch, M. (2018). An observationally based evaluation of subgrid scale ice thickness distributions simulated in a large-scale sea ice-ocean model of the Arctic Ocean. *J. Geophys. Res. Ocean.*, *123*(11), 8052–8067. doi: 10.1029/2018JC014022

Van Achter, G., Fichefet, T., Goosse, H., Pelletier, C., Sterlin, J., Huot, P. V., … Porter-Smith, R. (2022). Modelling landfast sea ice and its influence on ocean–ice interactions in the area of the Totten Glacier, East Antarctica. *Ocean Model.*, *169*(December 2020), 101920. doi: 10.1016/j.ocemod.2021.101920

Wang, Q., Marshall, J., Scott, J., Meneghello, G., Danilov, S., & Jung, T. (2019). On the feedback of ice-ocean stress coupling from geostrophic currents in an anticyclonic wind regime over the Beaufort Gyre. *J. Phys. Oceanogr.*, *49*(2), 369–383. doi: 10.1175/JPO-D-18-0185.1

World Meteorological Organization. (1970). *WMO sea-ice nomenclature. Terminology, codes and illustrated glossary* (Tech. Rep. No. 259). Geneva: World Meteorological Organization. (145 pp.)

Yabuki, H., Park, H., Kawamoto, H., Suzuki, R., Razuvaev, V., Bulygina, O., & Ohata, T. (2011). *Baseline Meteorological Data in Siberia (BMDS) Version 5.0, Arctic Data archive System (ADS).* Retrieved from `https://ads.nipr.ac.jp/dataset/A20131107-002`

Yu, Y., Stern, H., Fowler, C., Fetterer, F., & Maslanik, J. (2014). Interannual variability of arctic landfast ice between 1976 and 2007. *J. Clim.*, *27*(1), 227–243. doi: 10.1175/JCLI-D-13-00178.1

Zhai, M., Cheng, B., Leppäranta, M., Hui, F., Li, X., Demchev, D., … Cheng, X. (2021). The seasonal cycle and break-up of landfast sea ice along the northwest coast of Kotelny Island, East Siberian Sea. *J. Glaciol.*, 1–13. doi: 10.1017/jog.2021.85

Zhang, J., & Hibler, W. D. (1997). On an efficient numerical method for modeling sea ice dynamics. *J. Geophys. Res. Ocean.*, *102*(C4), 8691–8702. doi: 10.1029/96JC03744

Zhang, J., & Rothrock, D. A. (2003). Modeling global sea ice with a thickness and enthalpy distribution model in generalized curvilinear coordinates. *Mon. Weather Rev.*, *131*(5), 845–861. doi: 10.1175/1520-0493(2003)131⟨0845:MGSIWA⟩2.0.CO;2

Zhang, J., & Rothrock, D. A. (2005). Effect of sea ice rheology in numerical investigations of climate. *J. Geophys. Res. C Ocean.*, *110*(8), 1–15. doi: 10.1029/2004JC002599

Zhao, J., Cheng, B., Vihma, T., Heil, P., Hui, F., Shu, Q., . . . Yang, Q. (2020). Fast Ice Prediction System (FIPS) for land-fast sea ice at Prydz Bay, East Antarctica: an operational service for CHINARE. *Ann. Glaciol.*, *61*(83), 271–283. doi: 10.1017/aog.2020.46